Bath-limited dynamics of nuclear spins in solid-state spin platforms

Mykyta Onizhuk and Giulia Galli

Phys. Rev. B **108**, 075306 — Published 30 August 2023

DOI: 10.1103/PhysRevB.108.075306

Bath-limited dynamics of nuclear spins in solid-state spin platforms

Mykyta Onizhuk[1] and Giulia Galli[1,2,3,*]

[1]*Department of Chemistry, University of Chicago, Chicago, IL 60637, USA*

[2]*Pritzker School of Molecular Engineering, University of Chicago, Chicago, IL 60637, USA*

[3]*Materials Science Division and Center for Molecular Engineering, Argonne National Laboratory, Lemont, IL 60439, USA*

(Dated: August 21, 2023)

Abstract

Nuclear spins in the proximity of electronic spin defects in solids are promising platforms for quantum information processing due to their ability to preserve quantum states for a remarkably long time. Here we report a comprehensive *ab initio* study of the nuclear spin dynamics in solid-state systems. First, we characterize spin exchange-dependent oscillations of the Hahn-echo signal of the single nuclear spins in iso-nuclear spin baths pointing at a new sensing modality of dynamical-decoupling spectroscopy. Using first-principles simulations, we then quantify the enhancement in the coherence of nuclear spins as a function of distance and state of the electron spin and validate our results with experimental data for the nitrogen vacancy in diamond. Finally, we describe how hybridization of the electronic states suppresses the coherence time of strongly coupled nuclear spins and how dynamical changes of the electron spin state may deteriorate nuclear coherence. The computational framework developed in our work is general and can be broadly applied to predict the dynamical properties of nuclear spins in a wide variety of systems. Overall, our results elucidate many pitfalls that should be avoided to preserve the nuclear spin state in solid-state systems.

I. INTRODUCTION

Nuclear spins in solids and molecules can preserve their quantum state for a remarkably long time, exceeding seconds [1, 2] and even hours [3, 4], compared to the typical millisecond timescale of electronic spin defects [5, 6], due to their low magnetic moment. Hence nuclear spins are valuable resources for quantum information processing, including memory registers in quantum networks [2, 7–9], nuclei-assisted quantum sensors [10, 11] and components of fault-tolerant quantum processors [12, 13]. In particular, in the presence of electron spin qubits in semiconductors and insulators, the hyperfine interactions between the electron and nuclear spins allow for electron-spin assisted initialization and read-out [14–16], enabling full quantum control over the nuclear spin states.

Yet it still remains unclear what is limiting the coherence time of nuclear spins. While the coherence properties of the spin defects have been extensively investigated both experimentally [17–23] and theoretically [24–28], our understanding of the nuclear spin qubit dynamics

* gagalli@uchicago.edu.

is minimal. Acquiring a fundamental understanding of nuclear spin coherence in the proximity of electron spin qubits is crucial, e.g., to guide the design of nuclear spin environments for optimal performance of memory registers in quantum network applications [2, 5, 29].

First principles simulations represent promising techniques to investigate decoherence of the spin qubits in solids. From predicting bath spin-induced relaxation [30, 31], identifying new host materials [32, 33], and sensing modalities [34–37] to engineering spin environments [38–40], simulations have proved to be crucial in understanding spin-bath interactions in realistic systems. However to date, no attempt has been made to quantitatively characterize nuclear spin coherence processes in the presence of a spin defect using accurate computational methods. Such a characterization is challenging as one needs to account for weak correlated fluctuations of numerous bath spins, where the dominant interaction arises from the electron-nuclear spin coupling.

In this work, we use large-scale cluster-correlation expansion (CCE) calculations in conjunction with density functional theory (DFT) results to perform an *ab initio* study of nuclear spin coherence dynamics. We consider nuclear spins in the proximity of a state-of-the-art spin qubit platform, the negatively charged nitrogen vacancy in diamond (NV) [41, 42]. Our computational results for nuclear spin Hahn-echo and Ramsey coherence times are in excellent agreement with experimental data, bridging the gap between theory and experiment. Our calculations enable the precise mapping of the coherence times to the geometric positions of the nuclear spins, relative to the spin defect, and the identification of the primary sources of nuclear spin decoherence in a wide range of conditions. The decoherence channels identified in our work are general and our conclusions may be applied to any nuclear-electron spin coupled platforms. Overall, our work provides a robust approach to predict nuclear spin coherence dynamics for a variety of systems.

II. NUCLEAR SPIN IN A NUCLEAR SPIN BATH

We begin by investigating the coherence properties of a single nuclear spin coupled to an iso-nuclear spin bath.The properties of such nuclear spins can be measured in the experiment if the electron spin nearby has an even total spin (see section III). As an example, we consider a ^{13}C nucleus in diamond with natural isotopic abundance (Fig. 1a). We adopt two theoretical frameworks - the CCE approach [43], which assumes that decoherence arises

only from dephasing, and the generalized CCE approach (gCCE) [44], which accounts for both relaxation and dephasing of the central spin (see Appendix A for in-depth discussion on the methods).

Figure 1b shows the computed coherence time of the nuclear spins corresponding to Ramsey and Hahn-echo measurements in a high field limit. We find an excellent agreement between theory and experiment [45]. Ramsey calculations (Fig. 1c) converge at the 2nd order of the CCE (CCE2) and Hahn-echo results (Fig. 1d) converge at the 4th order [46]. The difference between Ramsey signals computed at the first and second order is small, indicating that the single bath spin dynamics dominates the decoherence process, as expected [25]. The order at which the Hahn-echo signal converges is significantly higher than that typically required to investigate the coherence time of electron spins (CCE2) [47–49], highlighting the need to account for higher-order correlations of the bath dynamics to accurately predict nuclear spin coherence times.

We find that both coherence times scale as the inverse of the nuclear spin concentration ($T_2,\ T_2^* \propto c^{-1}$) [46]. We note that the distributions of the inhomogeneous T_2^* and homogeneous spin dephasing times T_2 overlap in Fig. 1b, and the coherence enhancement from the refocusing pulse is on average small, a characteristic behavior of a broad noise spectrum [50].

However, the behaviour of the coherence function turns out to be much more complex than one might expect from classical stochastic noise models, where inter-nuclear interactions are simply treated as an effective nuclear spin field [51]. Only with a complete quantum-mechanical treatment can we uncover the complex oscillatory dynamics of the Hahn-echo signal (Fig 1d). The oscillations arise from the direct spin-exchange interactions with single spins in the environment: if one neglects the spin exchange (CCE framework), the coherent oscillations are not present in the Hahn-echo signal (Fig. 1d). Similar effects have been observed in the electron spin-echo envelope modulation (ESEEM) of electron-radical pairs in organic molecules [52, 53]. Contrary to the ESEEM arising from perpendicular hyperfine couplings [47], these oscillatory features do not disappear with increasing magnetic field.

To illustrate the physical origin of the spin-exchange-dependent modulations we derive an analytical expression for the Hahn-echo coherence function $\mathcal{L}(t) = \left(\langle \hat{I}_{x,0}(t)\rangle + i\langle \hat{I}_{y,0}(t)\rangle\right)$ of a central spin coupled to a single bath spin. We consider the following simplified Hamiltonian

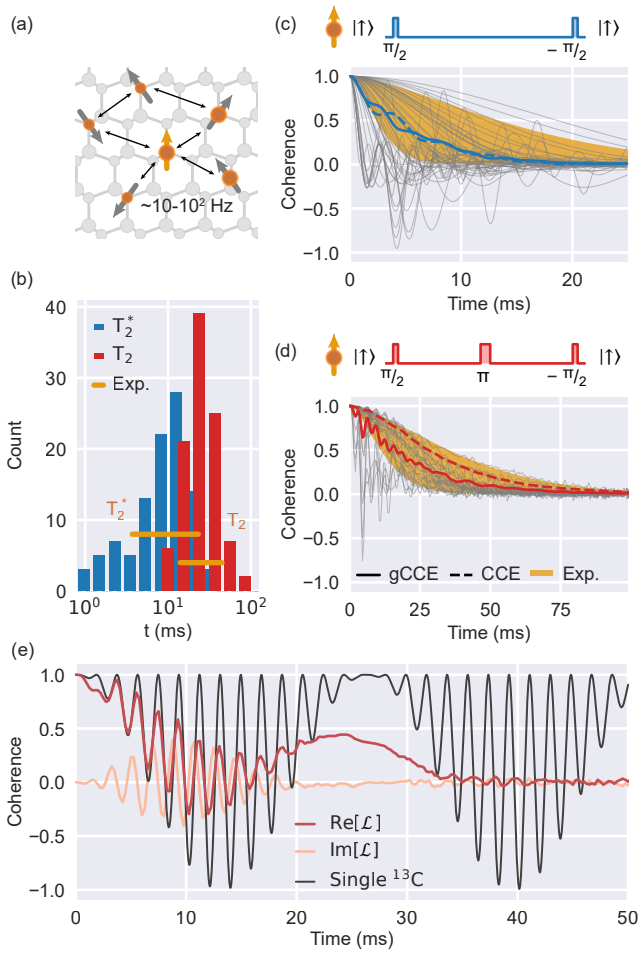

FIG. 1. (a) Schematic representation of a nuclear spin in a nuclear spin bath. (b) Distribution of Ramsey (T_2^*) and Hahn-echo (T_2) coherence times for nuclear spins computed with the gCCE approach. Horizontal bars show the range of experimental values[45]. (c (d)) Computed Ramsey (Hahn-echo) signals of the nuclear spins. The top diagram represents the sequence of pulses for each type of experiment. Each grey trace was obtained for a single random configuration and computed at the gCCE level of theory. Colored lines show ensemble-averaged coherence curve computed with the CCE (dashed line) and gCCE (solid line) methods. The applied magnetic field is 50 mT. (e) Real (red) and imaginary (orange) part of the Hahn-echo coherence function for a random bath configuration which contains a bath spin coupled to a central spin with $\sigma = 151$ Hz (Eq. 1) at a magnetic field of 0.05 mT. Analytical expression for $\langle \hat{I}_x \rangle$ of the system with only the central spin and a single bath spin shown in black (Eq. 2).

of the system:

$$\hat{H} = w_0 \hat{I}_{z,0} + w_1 \hat{I}_{z,1} + \frac{1}{2}\sigma(\hat{I}_{+,0}\hat{I}_{-,1} + h.c.) \tag{1}$$

where $\hat{I}_{i,0}$ and $\hat{I}_{i,1}$ are spin operators for the central spin and the bath spin respectively, w_0, w_1 are Larmor frequencies, and σ is the spin-exchange coupling. The presence of $\hat{I}_{z,0}\hat{I}_{z,1}$ type of couplings in the Hamiltonian leads to the same expression for the spin magnetization (see Eq. 2 and 3 below) and hence they were omitted in Eq. 1.

Assuming the initial state of the central spin is $|+X\rangle = \frac{1}{\sqrt{2}}(|\uparrow\rangle + |\downarrow\rangle)$ and the π-pulse applies a rotation around the x-axis, we obtain the following expressions for the spin magnetization:

$$\langle \hat{I}_{x,0}(t) \rangle = \frac{1}{2} - \frac{\sigma^2}{\Omega^2} \sin^2[\frac{\Omega t}{4}] \sin^2(\frac{(w_0 + w_1)t}{4}), \tag{2}$$

and

$$\langle \hat{I}_{y,0}(t) \rangle = \frac{\sigma^2}{2\Omega^2} \sin^2(\frac{\Omega t}{4}) \sin(\frac{(w_0 + w_1)t}{2}), \tag{3}$$

where $\Omega = \sqrt{(w_1 - w_0)^2 + \sigma^2}$. For a ^{13}C nuclear spin in a ^{13}C spin bath, Larmor frequencies are equal, $w_0 = w_1 = -\gamma_n B_z$, and the spin-exchange coupling arises from the dipolar interactions $\sigma = -P_{zz}$ (see Appendix A).

Hence, one can observe a strong out-of-phase signal $\langle \hat{I}_y(t) \rangle$ (Eq. (3) and Fig. 1e), which should be easily detectable in the experiment, providing a possible way to directly measure spin-exchange coupling between spins in solids. In contrast to existing methods that probe the nuclear spin pair dynamics with the sensor spin [54, 55], the echo oscillations characterized here require selective π-pulses and readout on one of the spins, but do not necessitate an auxiliary probing qubit.

Equations (1-3) assume the presence of a single bath spin with a coupling significantly stronger than its interactions with the remaining bath. Due to the same strength of interactions in the iso-nuclear spin bath and the stochastic nature of their spatial location, such assumptions are not always justified in the systems under study. However, the physical phenomena of the out-of-phase spin-echo oscillations depending on the exchange-type interaction is general, and will be present in the dynamical decoupling experiments whenever the spin qubit is coupled to the spin bath of the same type.

In addition, our calculations show that the role of longitudinal relaxation in determining the decoherence processes is highly dependent on the given nuclear spin configuration. Relaxation is negligible for some nuclear spins; for others, it completely determines the de-

coherence rate [46]. On average, the spin exchange with the environment accounts for about 40% of the decoherence rate for the ensemble of ^{13}C nuclear spins-½ (gCCE ensemble T_2 22.4(2) ms vs. CCE 36.66(9) ms) and 30% for single ones. The effect of higher spins is discussed in the supplementary information [46]. Thus, for each specific electronic spin defect present in a solid, one should perform a detailed search within all experimentally available nuclear spins to identify the ones best suited for quantum memories.

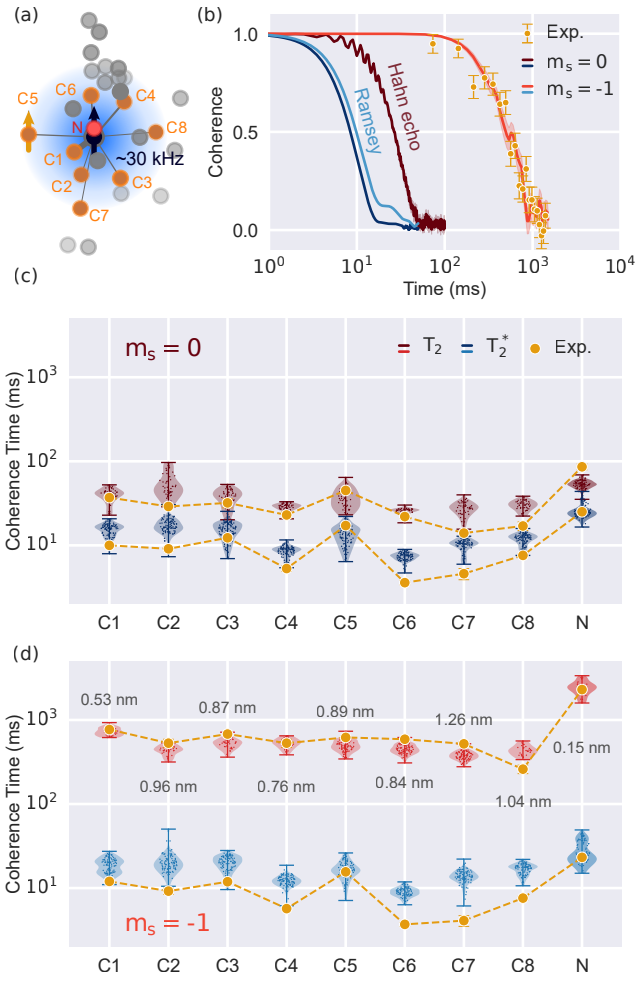

FIG. 2. (a) Graphical representation of the experimentally determined positions of 27 ^{13}C nuclear spins in proximity of an NV center in diamond from ref. [56]. Orange circles show nuclear spins with measured coherence times. (b) Coherence signals for the nuclear spin C5. Solid lines are theoretical predictions; yellow points are experimental data. (c (d)) T_2 and T_2^* of the nine nuclear spin registers measured by Bradley et al. [45] and represented by yellow lines when the NV is in the $m_s = 0$ ($m_s = -1$) state. Distributions correspond to computed coherence times in 50 random nuclear spin configurations around the 27 nuclear spins, identified in the experiment (see text). The Hahn echo is computed at the 4th (5th) order of the cluster expansion for the ^{13}C (^{14}N) nuclear spins.

III. NUCLEAR SPINS IN THE PRESENCE OF AN ELECTRON SPIN

Now we turn our attention to the properties of nuclear spins in the presence of an electron spin.

The CCE method up to the second order was previously used to qualitatively investigate the properties of the nuclear spins in proximity of shallow donors in Si [57]. Here we apply the fully converged CCE [43] and generalized CCE [44] schemes with so called "externally aware" cluster corrections [58] (See Appendix A) to quantitatively reproduce the experimental data.

We consider the NV center in diamond as a prototypical example of an electronic spin defect. With a total spin of 1, the NV center can be initialized in three eigenstates, which differ by the projection of the magnetic moment along the [111] axis of diamond ($m_s = -1, 0, 1$). By preparing the NV in the $m_s = 0$ state, one can, up to first order, eliminate the electron spin coupling to the spin bath and recover the same coherence time that nuclear spins exhibit in a pure nuclear spin bath (i.e, free nuclear spins). In the $m_s = -1, 1$ states, the NV center induces a strong hyperfine field on the nuclear spins, which dominates the inter-nuclear interactions. The hyperfine field gradient greatly suppresses the polarization transfer between different nuclei, leading to a significant change in the nuclear spin dynamics – an effect known as frozen core [57, 59].

A. Experimental validation of the computational protocol

We validate the predictions of our calculations by comparing our results with the experimental measurements of coherence times reported by T. H. Taminiau and coworkers [16, 45, 56]. The data for NV in $m_s = 0$ presents a new and previously unpublished data set obtained on the same NV center as used in these studies [60]. To apply π-pulses to the separate nuclear spins in the experiment, one has to include a short period of time during which the electron spin is in $m_s = -1$ state [46], which might lead to small discrepancies between the theoretical predictions and the experimental data.

We prepare a set of random configurations of nuclear spins placed around a cluster of 27 nuclear spins with experimentally identified positions [56] and compute the coherence of nine selected nuclear spins (C1-C8 and N in Fig. 2a). Using *ab initio* computed hyperfine parameters for randomly placed nuclear spins (see Appendix A), we obtain both Hahn-echo

and Ramsey coherence times of all nine nuclear registers.

Our calculations show that the presence of the electronic defect center greatly affects the nuclear spin qubit dynamics under the dynamical decoupling protocol. For example, in Fig. 2b, we show that the Hahn-echo coherence time of the C5 nuclear register is enhanced by a factor of 18 when the electron spin is in the $m_s = -1$ state. We also find a clear correlation between distance from the NV and the T_2 of the nuclear spins. Maximum T_2 values are achieved for the ^{14}N nuclear spin, which is located in the center of the frozen core and has a lower gyromagnetic ratio than that of ^{13}C.

The electron-nuclear spin interactions dominate the dynamics of the nuclear spin bath; thus, an accurate description of the nuclear spin's decoherence processes requires accounting for numerous weak correlated fluctuations of the bath spins. For the CCE calculations to converge, it was necessary to include on the order of 10^6 clusters of three and four nuclear spins in our Hahn-echo calculations for ^{13}C nuclear spins, and additionally 10^6 clusters of five for ^{14}N. In contrast to the results obtained for the free nuclear spin bath ($m_s = 0$), the Hahn echoes for the NV center in the $m_s = -1$ state are identical with both the CCE and gCCE methods [46], indicating a complete suppression of the spin relaxation process.

Unlike the Hahn echo, the Ramsey signal remains mostly unchanged when the electron is in the $m_s = -1$, compared to that of the free nuclear spins. The T_2^* is limited by the interactions with the small number of nearest bath spins [25]. We note that each experimental data falls well within the computed distribution (Fig. 1b); however the computed T_2^* is overestimated for specific nuclear spins, due to the fixed exclusion radius around the experimental cluster used to set up our model (see Appendix A). By varying this exclusion radius we can reproduce the experimental Ramsey coherence time for specific nuclear spins [46]. These results point at an amount of nuclear spins in the proximity of each of the registers which is larger than expected based on the number of experimentally identified positions [56].

Overall we find excellent agreement between experimental and computed values, thus validating the applicability and accuracy of our computational framework, even in the presence of the dominating hyperfine field of the electron spin.

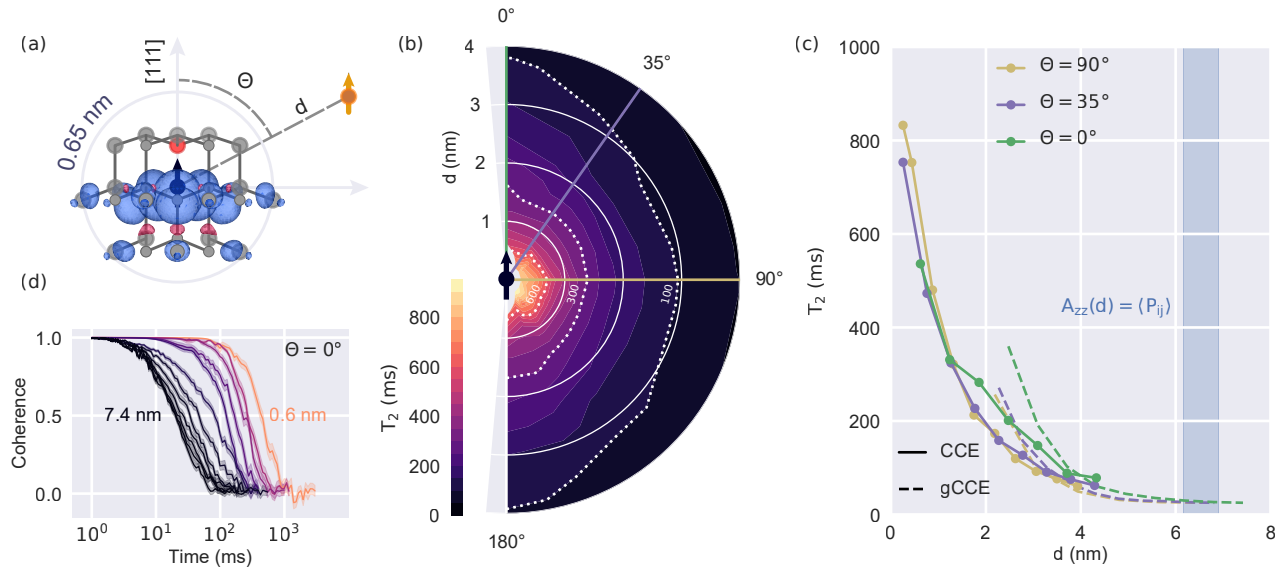

FIG. 3. (a) Spin density distribution around the NV center in diamond computed using DFT and the PBE functional. d is the distance from the NV center, the polar angle Θ is the angle between the NV axis and the position of the nuclei. (b) Computed ensemble-averaged T_2 as a function of the distance d from the NV center and the polar angle Θ. To simulate the high-field limit, the coherence time of the nuclear spins at distances ≤ 0.5 nm computed at the magnetic field of 1 T, for all other distances $B = 50$ mT. Dashed white lines show distances at which the T_2 is (from left to right) 600, 300, and 100 ms. (c) Computed T_2 of the nuclear spin at three polar angles $\Theta = 0°, 35°, 90°$. The generalized cluster expansion (gCCE) simulations (dashed line) were carried out using a smaller number of clusters than CCE, converged for free nuclear spin [46]. The value of d where the mean hyperfine coupling is equal to the mean internuclear coupling $A_{zz}(d) = \langle P_{ij} \rangle$ was computed as $\left| \frac{\gamma_e}{\gamma_n} \overline{r}_{ij}^3 \right|^{1/3}$ where $\overline{r}_{ij}$ is the mean internuclear distance (0.45-0.5 nm). (d) Computed ensemble-averaged Hahn echo as a function of the distance from the NV center for nuclear spins aligned along the [111] direction.

B. Coherence time of nuclear spins as a function of position

Having validated our computational framework, we now turn to investigating the dependence of the nuclear coherence time on the position and orientation of the nuclear spins inside the frozen core of the electron spin (Fig. 3a).

In Figure 3b, we report a complete map of the nuclear spins ensemble averaged T_2,

computed as a function of the polar angle Θ and the distance from the electron spin d, for the NV center in the $m_s = -1$ statein the limit of high magnetic field. The precise magnetic field at which the coherence time saturates depends on the location of the nuclear spin inside the frozen core. For the nuclear spins within 1 nm of the NV center, very strong magnetic fields are required, while for the further spins 50 mT is sufficient [46].

We find that T_2 ranges from more than 600 ms for nuclear spins within 0.5 nm of the electron spin to less than 50 ms for nuclear spins at distances larger than 4 nm. Figure 3c reports cuts along several polar angles, showing a strong dependence of the coherence time on the orientation of the nuclear spin with respect to the NV center.

At distances of 3-4 nm, we observe a crossover between the predicted values of the CCE and gCCE methods. In this regime, the hyperfine gradient still suppresses the direct spin exchange between the central nuclear spin and the bath; however the number of clusters one needs to include in the calculations is smaller than those required to evaluate the coherence time well within the frozen core. Thus, the CCE and gCCE results give similar values of the coherence time. At large distances, the direct spin exchange contributes significantly to the decoherence, and the smaller coherence time predicted with gCCE is more accurate than the CCE result.

The coherence time reaches its maximum for equatorial nuclear spins in the (111) plane, $\Theta = 90°$. In the vicinity of the NV, the distribution of computed T_2 values matches that of the spin density of the defect (Fig. 3a), and the nuclear spins located where the spin density is the highest exhibit the maximum coherence time. In contrast, the axial nuclear spins along the [111] axis have longer T_2 times at larger distances. The boundary of the enhanced coherence time region lies within approximately four to five nanometers from the NV center; this distance is comparable to the distance at which the average strength of the internuclear interactions ($\sim$ 60 Hz) matches that of the mean hyperfine coupling. A more quantitative analysis of the frozen core size is presented in the next section.

C. Frozen core size of the electron spin

To quantify the spatial extent of the frozen core of the electron spin, we propose a simplified spin pair-only model, where the size of the bath and spin-pair cutoff radii are obtained in the absence of the electron spin (See Appendix A for more details). We find that

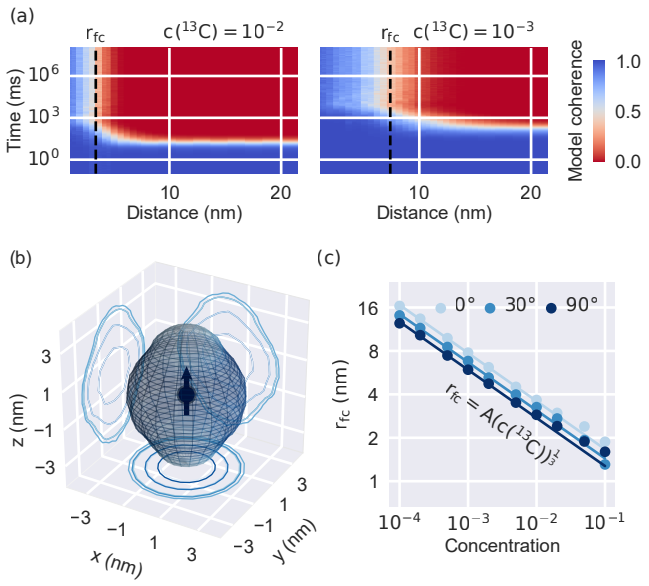

FIG. 4. (a) Spin-pair coherence function as a function of distance from the NV for two different isotopic concentrations. The frozen core radius r_{fc} is computed as the distance at which the model coherence function at time $\geq 10^6$ ms decreases to $1/e$ (b) Shape of the NV frozen core at natural isotopic concentration. (c) Scaling of the r_{fc} with ^{13}C concentrations at different polar angles Θ (See Fig. 3). Solid lines show fits to the function $r_{fc} = Ac^{-1/3}$.

within this approximation, the computed Hahn echo of the nuclear spins in the vicinity of the electron spin persists indefinitely. In the opposite limit of large distances between nuclear and electron spins, the model yields a coherence function decaying to zero, as expected (Fig. 4a). The distance from the electron at which the model coherence function changes its behavior from constant to decaying determines the boundary of the frozen core. Specifically, we define the frozen core radius (r_{fc}) as the distance at which the model coherence at an infinite time decreases to $1/e$.

Using this definition, we find that the frozen core of the NV center is asymmetrical and elongated along the z-axis (Fig. 4b). The radius r_{fc} varies from 2.7 nm at $\Theta = 55°$ to 3.8 nm at $\Theta = 180°$, matching the coherence time behavior shown in Fig 3c: the computed T_2 decays below 100 ms at 3.8 nm for axial and at 2.9 nm for equatorial spins nuclear spins. In contrast, the r_{fc} dependence on the azimuthal angle is negligible. The total volume of the frozen core is 165 nm^3, which corresponds to about 300 ^{13}C nuclear spins on average.

The frozen core size is correlated with the strength of the parallel component of the

hyperfine interaction with the electron spin. Within the point-dipole approximation, this interaction can be written as [61]:

$$A_{zz} = -\frac{\mathcal{G}}{r^3}(3\cos^2\Theta - 1) \tag{4}$$

Where $\mathcal{G} = \frac{\mu_0\gamma_e\gamma_n\hbar}{4\pi} = 7.60$ Hz nm^3 for ^{13}C nuclear spins. We note that for different systems (such as quantum dots in Si [57]), other terms might dominate the hyperfine interactions, and one can expect different shapes of the frozen core. Interestingly, at the angle $\arccos(1/\sqrt{3}) \approx 55°$ where the dipolar coupling vanishes, the value of $r_{fc} = 2.7$ nm is only slightly smaller than 2.8 nm, obtained for $\Theta = 90°$.

We find that the isotopic purification of the system leads to an increased size of the frozen core, where r_{fc} scales as the cubic root of the isotopic concentration in a wide range of spin densities (Fig. 4c). The ratio between r_{fc} at different polar angles remains constant. Such scaling means that the average number of nuclear spins inside the frozen core remains constant for most isotopic concentrations. Only at high concentrations (above two percent of ^{13}C), the scaling deviates from cubic, and then the actual electron spin density distribution and discrete lattice site positions should be taken into account.

D. Nuclear spin coherence in a strongly coupled hybrid electron-nuclear spins system

The results of the Sec. III B are valid when electron spin and nuclear spin states are fully decoupled (i.e., $\hat{S}_z$ and $\hat{I}_z$ commute with the total Hamiltonian). However, at ambient magnetic fields, this condition can be violated when nuclear spin is strongly coupled to the electron, significantly altering the nuclear spin dynamics.

As an example, we consider ^{13}C (Fig. 5a) belonging to the first shell of the NV center. We write the central spins Hamiltonian as:

$$\begin{aligned}\hat{H}_{en} = D\hat{S}_z^{\,2} + \gamma_e B_z \hat{S}_z + \gamma_n B_z \hat{I}_z + A_{zz}\hat{S}_z\hat{I}_z + \\ A_{xx}\hat{S}_x\hat{I}_x + A_{yy}\hat{S}_y\hat{I}_y + A_{xz}(\hat{S}_x\hat{I}_z + \hat{S}_z\hat{I}_x)\end{aligned} \tag{5}$$

Where $\hat{S}_i$, $\hat{I}_i$ are electron and nuclear spin operators, $D = 2.88$ GHz is the NV center zero-field splitting, γ_e, γ_n are electron and ^{13}C nuclear spin gyromagnetic ratios respectively (see Appendix A for the full description). $A_{xx} = 99.8$ MHz, $A_{yy} = 176.8$ MHz, $A_{zz} = 108.0$ MHz,

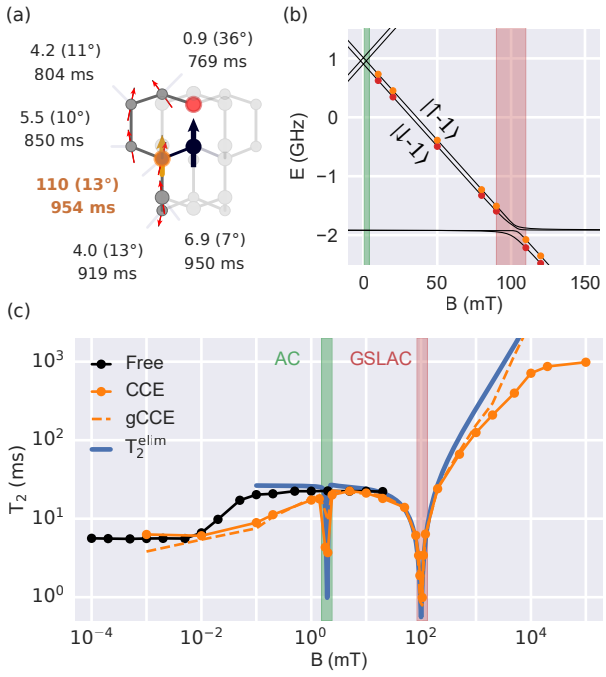

FIG. 5. (a) Computed first and second shell ensemble-averaged nuclear spin coherence times. For each nuclear spin, we also report the hyperfine coupling $\tilde{A}_{zz} = \sqrt{A_{xz}^2 + A_{zz}^2}$ in MHz, the angle Θ_A between the [111] axis of diamond and the hyperfine quantization axis, and T_2 computed in the limit of a large magnetic field. For the first shell nuclear spin (highlighted in orange), the coherence time is computed at 10 T, and for all others at 1T. Red arrows show hyperfine quantization axes. (b) Energy levels of the hybrid electron-nuclear spins system for NV and first shell nuclear spin as a function of an applied magnetic field along the [111] direction. Orange and red dots correspond to $|0_a\rangle$ and $|1_a\rangle$ levels respectively (see text). (c) Coherence time of the first-shell ^{13}C as a function of the applied magnetic field along the [111] axis, computed with CCE (solid orange line), gCCE (dashed orange line), and hybridization-limited T_2^{elim} (blue line, see text). T_2 for the free nuclear spin (black) is shown as a comparison. The green shaded region denotes avoided crossing (AC) in the electronic levels due to the hyperfine interactions; the red shaded region denotes ground state level anticrossing (GSLAC) of the electronic levels.

$A_{xz} = 25.5$ MHz are hyperfine couplings obtained from DFT calculations and are in good agreement with experimental data [62]. The energy levels of the combined electron-nuclear spins system are shown in Figure 5b.

We find that to obtain saturation of the coherence time of the first shell ^{13}C, a much

higher magnetic field is required than in the case of free nuclear spins (Fig. 5c). Strikingly, at all other applied fields, the nuclear spin T_2 is severely affected by the partial hybridization of the electronic spin levels induced by the hyperfine coupling. To analyze this effect, we express the two energy levels $|0_a\rangle$ and $|1_a\rangle$ of the hybrid electron-spin nuclear spin system as:

$$|1_a\rangle = |-1\uparrow\rangle + \alpha^{1a}_{-1\downarrow}\,|-1\downarrow\rangle + \alpha^{1a}_{0\uparrow}\,|0\uparrow\rangle + \alpha^{1a}_{0\downarrow}\,|0\downarrow\rangle \tag{6}$$

$$|0_a\rangle = |-1\downarrow\rangle + \alpha^{0a}_{-1\uparrow}\,|-1\uparrow\rangle + \alpha^{0a}_{0\uparrow}\,|0\uparrow\rangle + \alpha^{0a}_{0\downarrow}\,|0\downarrow\rangle \tag{7}$$

In the secular limit of $B_z \to \infty$, the amplitudes $\alpha^{1a}_{0\uparrow}$, $\alpha^{1a}_{0\downarrow}$ and $\alpha^{0a}_{0\uparrow}$, $\alpha^{0a}_{0\downarrow}$ that account for the hybridization of electron spin states, vanish [63, 64]. In the non-secular regime, these amplitudes can be computed by directly diagonalizing the Hamiltonian or from perturbation theory.

If the reduced density matrices of the electron spin in states $|0_a\rangle$ and $|1_a\rangle$ differ substantially, we expect a significant impact of the mixing of electron spin levels on the nuclear spin coherence time. To estimate the effect on T_2 of the difference in hybridization between the $|0_a\rangle$ and $|1_a\rangle$ levels, we use a modified approximate model first suggested in Ref. [65]. The model was first proposed to predict the T_2 of two electron-spin states with similar magnetization in the high-field regime, when slow oscillations of nuclear spin pairs dominate the decoherence process. Using such a model, we can express the contribution to the *nuclear spin* coherence time arising only from the electronic hybridization (which we denote as electron-limited, (elim)) as:

$$T_2^{\text{elim}}(B) \approx \mathcal{C}\frac{||P_{0a}(B)|| + ||P_{1a}(B)||}{||P_{0a}(B) - P_{1a}(B)||}, \tag{8}$$

where $P_{0a}(B) = \langle 0_a|\,\mathbf{S}\,|0_a\rangle$, $P_{1a}(B) = \langle 1_a|\,\mathbf{S}\,|1_a\rangle$ are the effective magnetization of the electron spin in the $|0_a\rangle$ and $|1_a\rangle$ states respectively, $\mathcal{C}$ is a magnetic field-independent constant, specific to a given system. We find $\mathcal{C}$ to be equal to 0.31 ms for the parameter range appropriate for the system under study [46]. The electron-limited coherence obtained from the model agrees well with the predictions of the full quantum mechanical treatment over a wide range of magnetic fields, thus confirming the significant impact of the hybridization of the electron spin levels on the coherence time of nuclear spins.

Using perturbation theory, we obtain an approximate expression for the electron spin-limited coherence time [46]:

$$T_2^{\text{elim}}(B) \approx \frac{4\mathcal{C}(D+\gamma_e B)(A_{zz}+\gamma_n B)}{A_{xz}(A_{xx}+2A_{zz}+2\gamma_n B)} \tag{9}$$

We find that T_2^{elim} is proportional to $\tan^{-1}(\Theta_A)$ at intermediate magnetic fields, where Θ_A is the angle between the hyperfine quantization axis $\mathbf{n} = A_{xz}\mathbf{i} + A_{yz}\mathbf{j} + A_{zz}\mathbf{k}$ and the [111] direction of the diamond lattice. For the first shell ^{13}C, the angle is equal to $\Theta_A = 13^\circ$ (Fig. 5a). Our results show that the T_2 of any nuclear spin with a substantial perpendicular component of the hyperfine coupling requires a significantly higher magnetic field to achieve saturation when the electron spin is in $m_s = -1$ state. One can use Eq. 9 to estimate the conditions at which the impact of the hybridization of the electron spin levels on nuclear spin T_2 becomes insignificant.

The effect of the partial hybridization of electron spin levels has the highest impact near avoided crossings of energy levels. In the case of electron spins, avoided crossings originating from hyperfine interactions lead to a decoherence-protected subspace [66]. Instead, the effect of these transitions on the T_2 of nuclear spins is extremely detrimental. At each of the avoided crossings, our calculations show a sharp dip in the coherence time of strongly coupled nuclear spins, highlighting the important trade-off one faces in utilizing nuclear spins as memory qubits at avoided crossings [14].

E. Effect of electron spin control on nuclear spin coherence

Having analyzed the characteristics of nuclear spin coherence times in the vicinity of an electron spin as a function of m_s, we now investigate how nuclear spin coherence is affected by *changes* in the state of the electronic spin. The dynamical change of the state of the electron spin has been shown to be a valuable tool for improving nuclear spin coherence. For example, one can use unbalanced echo [67] by applying control pulses to the electron spin to enhance the protection of the nuclear spin ensembles against lattice strain noise.

We analyze the effect of the central spin coherent control on nuclear spin coherence by applying a sequence of π_e-pulses (here, the index e denotes electron spin) to the NV center and we compute the dynamics of nuclear spins at two distances from the electron.

Figure 6a shows the nuclear spin coherence when a single π_e-pulse is applied to the electron

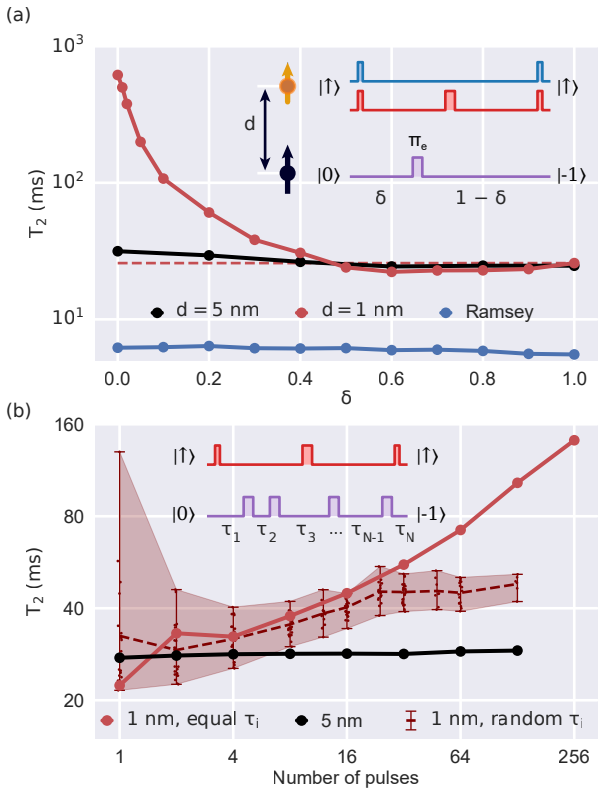

FIG. 6. (a) Pulse sequences and the corresponding computed nuclear spin T_2 (black and red) and T_2^* (blue) for a single nuclear spin at distances 1 nm and 5 nm from the NV center when a single π_e pulse is applied to the electron spin. The dark blue (orange) arrow represents an electron (nuclear) spin. T_2^* is shown for d = 1 nm.(b) Pulse sequence and the nuclear spin T_2 when many π_e pulses are applied to the electron spin. Red color shows T_2 of the nuclear spin at 1 nm. Spacing between the pulses (τ_i) is either random (points inside shaded area) or constant (solid line). Black line shows T_2 of the nuclear spin at 5 nm. Coherence time is computed at a 50 mT magnetic field using CCE at $\delta < 0.05$ and gCCE everywhere else.

spin at different fractions of the total time $0 \leq \delta \leq 1$. The electron spin is initialized in the $m_s = 0$ state; after the π_e-pulse is applied, the electron spin rotates into the $m_s = -1$ state. Before the π_e pulse, the nuclear spin precesses with frequency $w_L^{(0)} = -\gamma_n B$; upon the application of the pulse, the frequency is $w_L^{(-1)} = -\gamma_n B - A_{zz}$, leading to the emergence of a nonzero phase of the Hahn-echo signal. In our calculations, we obtain the decay of the coherence time from the absolute value of the coherence function $|\mathcal{L}|$.

We find that the coherence time of the nuclear spins outside the frozen core does not

change significantly with the state of the central spin. However, within the frozen core, the change is drastic: when $\delta > 0.5$, the nuclear spin coherence time reaches a local minimum and we observe a 15% drop in T_2, compared to that of the spin in the $m_s = 0$ state, indicating a destructive interference between nuclear and electron control pulses.

Figure 6b shows the T_2 of the nuclear spin as a function of the number of applied π_e pulses. The electron spin is initialized in the $m_s = 0$ state. In this case, one can achieve a so-called motional narrowing of the hyperfine field [14]: as the number of π_e pulses increases, the electron-induced field rapidly oscillates and its overall effect can be described by an average field. The motional narrowing leads to a significant enhancement in coherence time. We obtain the highest increase in T_2 for a constant spacing between π_e pulses; however, T_2 is still much smaller than the coherence time achieved when the electron spin remains in the $m_s = -1$ state (620 ms).

IV. DISCUSSION AND OUTLOOK

In this work, we presented and validated a robust computational protocol to describe the nuclear spin dynamics in a nuclear spin bath. Using the proposed protocol, we determined the main noise channels affecting the coherent lifetime of nuclear memories in spin defect systems. In the absence of electron spins, nuclear spin coherence is limited almost equally by dephasing and relaxation processes. However, the interplay between these two processes greatly varies depending on the specific spatial configuration of nuclear spins. This finding indicates that the geometrical arrangements of the nuclear spin environment of spin defects should be carefully characterized [56], in order to identify the optimal nuclear spins to store nuclear quantum states as long as possible.

Our calculations showed that the Hahn echo of single nuclear spins exhibit complex oscillatory features emerging from the spin exchange interactions with the bath. These oscillations arise from the direct interactions between a single bath spin and the central spin, and they have potential to be used to identify and characterize spin exchange interactions with the bath.

In the presence of electron spins, we characterized the shape of the frozen core of nuclear spins around the defect with a spin-pair model. The core turns out to be oblong and elongated along the z-axis, matching the dependence of the dipolar hyperfine coupling on

the polar angle. The volume of the frozen core is inversely proportional to the concentration of nuclear spins; thus, the total number of nuclear spins inside the frozen core is constant and equal to about 300 ^{13}C, irrespective of any isotopic purification. This value sets a precise boundary on how many ^{13}C nuclear spins it is possible to interact with and, therefore, sense or control using a single NV center.

We analyzed the frozen core effect on coherence time and found that the Hahn-echo T_2 of the nuclear spins can be enhanced by up to 36 times for the closest nuclear spins, when an electron is in the $m_s = -1$ state. Near an NV center, the highest T_2 is attained by equatorial nuclear spins, closely matching the spin density distribution of the NV center. Further away from the electronic spin defect, it is the polar nuclear spins that retain the highest T_2.

However, in strongly coupled nuclear-electron spin systems, the hyperfine-induced hybridization of electron spin levels acts as a major source of decoherence at commonly used range of magnetic fields. This decoherence channel is most prominent near avoided crossings between energy levels. We find that the prohibitively high magnetic fields would be necessary to suppress the impact of partial hybridization of electron spin states on coherence time in the strong coupling regime.

Finally, we uncovered that the coherent control of the electron magnetic states severely impacts the nuclear spin coherence time inside the frozen core. Even with no noise affecting the electron spin, we find that the nuclear T_2 is dramatically decreased as soon as the state of the electron is changed.

Overall, the validated computational framework proposed here for the study of nuclear spin registers is general and applicable to broad classes of systems and problems. For example, one can use the proposed platform to study the impact of the total spin of an electron qubit on the frozen core effect. In particular, one could investigate the difference in coherence times in the presence of electron spin-$^1/_2$ qubits, exhibiting a hyperfine field in any state, and NV centers, where one of the magnetic states does not exert a hyperfine field. Importantly, using our computational platform one may screen materials for optimal nuclear spin coherence times [32].

Another interesting avenue of research is the exploration of the predicted frozen core size and shape as an engineering tool for the bottom-up design of spin qubits in molecular systems [68]. With each frozen core corresponding to a computational domain of a specific electron spin, one can envision a nanoscale network of spin processors, with electron spins

as processing units and nuclear spins acting as memory qubits.

Finally, our results tell a series of cautionary tales for the applications of nuclear spins for quantum technologies. From the applied magnetic field to the electron spin control, we elucidated the various noise channels that may adversely affect the quantum state of the nuclear spins.

V. ACKNOWLEDGEMENTS

This work was supported by the Design and Optimization of Synthesizable Materials with Targeted Quantum Characteristics (AFOSRFA9550-19-1-0358). M.O. acknowledges the support of a Google PhD Fellowship. We thank C. E. Bradley and T. H. Taminiau for providing the experimental data, and C.P. Anderson, M. Raha, Y. Wang for useful comments.

Appendix A: Computational framework

The quantum evolution of the combined electron spin-nuclear register is described by the model Hamiltonian:

$$\hat{H} = \hat{H}_{en} + \hat{H}_{en\text{-}b} + H_b \tag{A1}$$

The central spin Hamiltonian $\hat{H}_{en}$ includes:

$$\hat{H}_{en} = D\hat{S}_z + \gamma_e \mathbf{B}\cdot\mathbf{S} + \gamma_n \mathbf{B}\cdot\mathbf{I}_0 + \mathbf{S}\cdot\mathbf{A}_0\cdot\mathbf{I}_0 \tag{A2}$$

Here D is the zero field splitting of the electron spin, $\mathbf{B} = (B_x, B_y, B_z)$ is the magnetic field, γ_n is the gyromagnetic ratio of the ^{13}C nuclear spin, $\mathbf{S} = (\hat{S}_x, \hat{S}_y, \hat{S}_z)$ and $\mathbf{I}_i = (\hat{I}_{x,i}, \hat{I}_{y,i}, \hat{I}_{z,i})$ denote electron and the i-th nuclear spin operators, respectively. The zero index denotes a given nuclear spin chosen as a qubit.

The bath-central spins Hamiltonian $\hat{H}_{en\text{-}b}$ and the bath Hamiltonian $\hat{H}_b$ are defined as follows:

$$\hat{H}_{en\text{-}b} = \sum_i \mathbf{S}\cdot\mathbf{A}_i\cdot\mathbf{I}_i + \mathbf{I}_0\cdot\mathbf{P}_{0i}\cdot\mathbf{I}_i, \tag{A3}$$

and

$$\hat{H}_b = \sum_i -\gamma_n \mathbf{B} \cdot \mathbf{I}_i + \sum_{i \geq j} \mathbf{I}_i \cdot \mathbf{P}_{ij} \cdot \mathbf{I}_j \tag{A4}$$

.

Here $\mathbf{A}_i$ is the hyperfine coupling tensor of the i-th nuclear spin, and $\mathbf{P}_{ij}$ is the dipole-dipole coupling between spins i and j.

We use the cluster-correlation expansion (CCE) to compute the coherence function of the nuclear spin, defined as:

$$\mathcal{L}(t) = \frac{\langle \hat{I}_-(t) \rangle}{\langle \hat{I}_-(0) \rangle} = \frac{\langle \uparrow | \, \hat{\rho}(t) \, | \downarrow \rangle}{\langle \uparrow | \, \hat{\rho}(0) \, | \downarrow \rangle} \tag{A5}$$

where $|\uparrow\rangle$ and $|\downarrow\rangle$ are nuclear spin-up and spin-down states and $\hat{I}_-$ are nuclear lowering spin operators, $\hat{\rho}(t)$ is the density matrix of the central spin. In the presence of an NV center we define off-diagonal elements between eigenstates of $\hat{H}_{en}$ corresponding to the diabatic levels $|\uparrow 0\rangle$, $|\downarrow 0\rangle$ for $m_s = 0$, and to $|\uparrow -1\rangle$, $|\downarrow -1\rangle$ for $m_s = -1$ cases.

Within the CCE scheme, the coherence function $\mathcal{L}(t)$ is factorized into the contributions of bath spin clusters with different size [43]:

$$\mathcal{L}(t) = \prod_i \tilde{L}^{\{i\}} \prod_{i,j} \tilde{L}^{\{ij\}} ... \tag{A6}$$

The contributions are computed recursively from the coherence function of the central spin, interacting with only a given cluster C as $\tilde{L}_C = \frac{L_C}{\prod_{C'} \tilde{L}_{C' \subset C}}$, where the subscript C' indicates all sub-clusters of C.

Depending on the framework, the L_C are computed as follows. In conventional CCE [43, 69] (referred throughout the text as CCE), the relaxation processes of the central spin are discarded, and the coherence function is computed as an overlap in the cluster evolution, dependent on the central spins state:

$$L_C = \langle C | \, \hat{U}_C^{(0)}(t) \hat{U}_C^{(1)\dagger}(t) \, | C \rangle \tag{A7}$$

Where $|C\rangle$ is the initial state of the cluster C. $\hat{U}_C^{(\alpha)}(t)$ is the time propagator defined in terms of the effective Hamiltonian $\hat{H}_C^{(\alpha)}$ conditioned on the qubit levels. Up to the second order of perturbation theory it can be written as:

$$\hat{H}_C^{(\alpha)} = \langle \alpha | \, \hat{H}_C \, | \alpha \rangle + \sum_{i \neq \alpha} \frac{\langle \alpha | \, \hat{H}_b \, | i \rangle \, \langle i | \, \hat{H}_b \, | \alpha \rangle}{E_\alpha - E_i} \tag{A8}$$

Where $|\alpha\rangle$, $|i\rangle$ are eigenstates of the central spins Hamiltonian $\hat{H}_{en}$, $\hat{H}_C$ is the Hamiltonian in Eq. (A2) including only the bath spins in the cluster C:

$$\hat{H}_C = \hat{H}_{en} + \hat{H}_{en\text{-}b}^{(i\in C)} + \hat{H}_b^{(i,j\in C)} \tag{A9}$$

In contrast, in the generalized CCE (gCCE) we compute the cluster contributions from the respective elements of the reduced density matrix of the central spin as [44]:

$$L_C = \langle a| \operatorname{Tr}_C[\hat{\rho}_{en\otimes C}(t)] |b\rangle , \tag{A10}$$

where $\rho_{en\otimes C}(t)$ is the density matrix of the system, which includes bath spins in the cluster C and all central spins. The evolution is computed using the full cluster Hamiltonian $\hat{H}_C$.

All π-pulses are assumed to be ideal, instantaneous, and selective to the spin chosen as a central one.

The strength of interactions between central nuclear spin and bath spins is very similar in the system under study, making the convergence of the expansion order particularly challenging. Here, we use Monte Carlo sampling of bath states [44], and for each pure bath state, we use "externally aware" cluster expansion by adding Izing-type coupling with the bath spins outside of the given cluster in a mean-field way. This approach has been shown to improve the convergence of the CCE method in the all-dipolar spin systems [58].

We use the PyCCE module [70] to carry out all CCE simulations. To approximate the dipolar coupling parameters, we use the actual spin density of the NV center in diamond, computed with density functional theory at the PBE [71] level in a 1000 atoms supercell using the Quantum Espresso package [72]. The dipolar coupling is then computed as [73]:

$$A_{ab} = \frac{1}{2}\frac{\mu_0}{4\pi}\gamma_e\gamma_n\hbar^2 \int \frac{|\mathbf{r}|^2\delta_{ab} - 3\mathbf{r}_a\mathbf{r}_b}{|\mathbf{r}|^5}\rho_s(\mathbf{r})d\mathbf{r} \tag{A11}$$

Where $\mathbf{r}$ is the position relative to a given nuclear spin, ρ_s is the electron spin density.

The contact terms of the nuclear spins at distances under 1 nm were computed using the GIPAW module of Quantum Espresso. For every other nuclear spin we assumed the contact terms to be vanishing.

To approximate the experimental nuclear spin bath we generated 50 random bath configurations around the experimental cluster. Assuming that all closest nuclear spins were identified in the experiment, we imposed a cutoff of 0.56 nm around each of the identified

nuclear spins. This cutoff is chosen so that the exclusion volume on average contains 27 nuclear spins.

To characterize the extent of the frozen core, we implement the following procedure. We use the coherence of the nuclear spin (test spin), computed with the CCE2 (the spin-pair model, similar to ref. [57]) as a criterion to decide whether the test spin is inside the frozen core. We first estimate how many spins and spin pairs around the nucleus contribute to its decoherence in the absence of electron spins, by using the spin-pair model. The number of spin pairs is determined via convergence of the model coherence function with the size of the bath (`r_bath`) and the cutoff radius (`r_dipole`) [70]. Using this number of spin pairs, we compute the dynamics of this hypothetical test spin at various distances from the electron spin. When the test spin is far away from the electron spin, the predicted model coherence function matches that of a test spin in the absence of the electron spin. The model coherence of the test spin in the vicinity of the electron spin, computed using the same number of pairs, is a constant (see Fig. 4a). The distance at which the model coherence function changes its behavior from constant to decaying function of time corresponds to the boundary of the frozen core. Therefore, at very long times ($t > 10^6$ ms), the model coherence (L_∞) is 1 near the electron spin and 0 outside of the frozen core. By fitting this coherence function at infinite time to a stretched exponential ($L_\infty = \exp(-(d/r_{fc})^n)$), we recover the size of the frozen core r_fc.

---

[1] P. C. Maurer, G. Kucsko, C. Latta, L. Jiang, N. Y. Yao, S. D. Bennett, F. Pastawski, D. Hunger, N. Chisholm, M. Markham, D. J. Twitchen, J. I. Cirac, and M. D. Lukin, Room-temperature quantum bit memory exceeding one second, Science **336**, 1283 (2012).

[2] C. E. Bradley, S. W. de Bone, P. F. W. Möller, S. Baier, M. J. Degen, S. J. H. Loenen, H. P. Bartling, M. Markham, D. J. Twitchen, R. Hanson, D. Elkouss, and T. H. Taminiau, Robust quantum-network memory based on spin qubits in isotopically engineered diamond, npj Quantum Information **8**, 10.1038/s41534-022-00637-w (2022).

[3] K. Saeedi, S. Simmons, J. Z. Salvail, P. Dluhy, H. Riemann, N. V. Abrosimov, P. Becker, H.-J. Pohl, J. J. L. Morton, and M. L. W. Thewalt, Room-temperature quantum bit storage exceeding 39 minutes using ionized donors in silicon-28, Science **342**, 830 (2013).

[4] M. Zhong, M. P. Hedges, R. L. Ahlefeldt, J. G. Bartholomew, S. E. Beavan, S. M. Wittig, J. J. Longdell, and M. J. Sellars, Optically addressable nuclear spins in a solid with a six-hour coherence time, Nature **517**, 177 (2015).

[5] A. Bourassa, C. P. Anderson, K. C. Miao, M. Onizhuk, H. Ma, A. L. Crook, H. Abe, J. Ul-Hassan, T. Ohshima, N. T. Son, G. Galli, and D. D. Awschalom, Entanglement and control of single nuclear spins in isotopically engineered silicon carbide, Nature Materials 10.1038/s41563-020-00802-6 (2020).

[6] G. Wolfowicz, F. J. Heremans, C. P. Anderson, S. Kanai, H. Seo, A. Gali, G. Galli, and D. D. Awschalom, Quantum guidelines for solid-state spin defects, Nature Reviews Materials **6**, 906 (2021).

[7] M. Pompili, S. L. N. Hermans, S. Baier, H. K. C. Beukers, P. C. Humphreys, R. N. Schouten, R. F. L. Vermeulen, M. J. Tiggelman, L. dos Santos Martins, B. Dirkse, S. Wehner, and R. Hanson, Realization of a multinode quantum network of remote solid-state qubits, Science **372**, 259 (2021), https://www.science.org/doi/pdf/10.1126/science.abg1919.

[8] M. Ruf, N. H. Wan, H. Choi, D. Englund, and R. Hanson, Quantum networks based on color centers in diamond, Journal of Applied Physics **130**, 070901 (2021), https://doi.org/10.1063/5.0056534.

[9] S. L. N. Hermans, M. Pompili, H. K. C. Beukers, S. Baier, J. Borregaard, and R. Hanson, Qubit teleportation between non-neighbouring nodes in a quantum network, Nature **605**, 663 (2022).

[10] Y. Matsuzaki, T. Shimo-Oka, H. Tanaka, Y. Tokura, K. Semba, and N. Mizuochi, Hybrid quantum magnetic-field sensor with an electron spin and a nuclear spin in diamond, Phys. Rev. A **94**, 052330 (2016).

[11] Z. Qiu, U. Vool, A. Hamo, and A. Yacoby, Nuclear spin assisted magnetic field angle sensing, npj Quantum Information **7**, 10.1038/s41534-021-00374-6 (2021).

[12] X. Rong, J. Geng, F. Shi, Y. Liu, K. Xu, W. Ma, F. Kong, Z. Jiang, Y. Wu, and J. Du, Experimental fault-tolerant universal quantum gates with solid-state spins under ambient conditions, Nature Communications **6**, 10.1038/ncomms9748 (2015).

[13] J. Casanova, Z.-Y. Wang, and M. B. Plenio, Noise-resilient quantum computing with a nitrogen-vacancy center and nuclear spins, Phys. Rev. Lett. **117**, 130502 (2016).

[14] A. Ruskuc, C.-J. Wu, J. Rochman, J. Choi, and A. Faraon, Nuclear spin-wave quantum

register for a solid-state qubit, Nature **602**, 408 (2022).

[15] M. T. Madzik, S. Asaad, A. Youssry, B. Joecker, K. M. Rudinger, E. Nielsen, K. C. Young, T. J. Proctor, A. D. Baczewski, A. Laucht, V. Schmitt, F. E. Hudson, K. M. Itoh, A. M. Jakob, B. C. Johnson, D. N. Jamieson, A. S. Dzurak, C. Ferrie, R. Blume-Kohout, and A. Morello, Precision tomography of a three-qubit donor quantum processor in silicon, Nature **601**, 348 (2022).

[16] M. H. Abobeih, Y. Wang, J. Randall, S. J. H. Loenen, C. E. Bradley, M. Markham, D. J. Twitchen, B. M. Terhal, and T. H. Taminiau, Fault-tolerant operation of a logical qubit in a diamond quantum processor, Nature **606**, 884 (2022).

[17] L. Childress, M. V. G. Dutt, J. M. Taylor, A. S. Zibrov, F. Jelezko, J. Wrachtrup, P. R. Hemmer, and M. D. Lukin, Coherent dynamics of coupled electron and nuclear spin qubits in diamond, Science **314**, 281 (2006), https://www.science.org/doi/pdf/10.1126/science.1131871.

[18] N. Mizuochi, P. Neumann, F. Rempp, J. Beck, V. Jacques, P. Siyushev, K. Nakamura, D. J. Twitchen, H. Watanabe, S. Yamasaki, F. Jelezko, and J. Wrachtrup, Coherence of single spins coupled to a nuclear spin bath of varying density, Phys. Rev. B **80**, 041201 (2009).

[19] P. L. Stanwix, L. M. Pham, J. R. Maze, D. Le Sage, T. K. Yeung, P. Cappellaro, P. R. Hemmer, A. Yacoby, M. D. Lukin, and R. L. Walsworth, Coherence of nitrogen-vacancy electronic spin ensembles in diamond, Phys. Rev. B **82**, 201201 (2010).

[20] E. Bauch, S. Singh, J. Lee, C. A. Hart, J. M. Schloss, M. J. Turner, J. F. Barry, L. M. Pham, N. Bar-Gill, S. F. Yelin, and R. L. Walsworth, Decoherence of ensembles of nitrogen-vacancy centers in diamond, Phys. Rev. B **102**, 134210 (2020).

[21] P. Jamonneau, M. Lesik, J. P. Tetienne, I. Alvizu, L. Mayer, A. Dréau, S. Kosen, J.-F. Roch, S. Pezzagna, J. Meijer, T. Teraji, Y. Kubo, P. Bertet, J. R. Maze, and V. Jacques, Competition between electric field and magnetic field noise in the decoherence of a single spin in diamond, Phys. Rev. B **93**, 024305 (2016).

[22] J. R. Maze, A. Dréau, V. Waselowski, H. Duarte, J.-F. Roch, and V. Jacques, Free induction decay of single spins in diamond, New Journal of Physics **14**, 103041 (2012).

[23] N. Bar-Gill, L. Pham, C. Belthangady, D. L. Sage, P. Cappellaro, J. Maze, M. Lukin, A. Yacoby, and R. Walsworth, Suppression of spin-bath dynamics for improved coherence of multi-spin-qubit systems, Nature Communications **3**, 10.1038/ncomms1856 (2012).

[24] J. R. Maze, J. M. Taylor, and M. D. Lukin, Electron spin decoherence of single nitrogen-

vacancy defects in diamond, Phys. Rev. B **78**, 094303 (2008).

[25] N. Zhao, S.-W. Ho, and R.-B. Liu, Decoherence and dynamical decoupling control of nitrogen vacancy center electron spins in nuclear spin baths, Phys. Rev. B **85**, 115303 (2012).

[26] Z.-H. Wang and S. Takahashi, Spin decoherence and electron spin bath noise of a nitrogen-vacancy center in diamond, Phys. Rev. B **87**, 115122 (2013).

[27] S. Ajisaka and Y. B. Band, Decoherence of three-level systems: Application to nitrogen-vacancy centers in diamond near a surface, Phys. Rev. B **94**, 134107 (2016).

[28] H. Park, J. Lee, S. Han, S. Oh, and H. Seo, Decoherence of nitrogen-vacancy spin ensembles in a nitrogen electron-nuclear spin bath in diamond, npj Quantum Information **8**, 10.1038/s41534-022-00605-4 (2022).

[29] S. Wehner, D. Elkouss, and R. Hanson, Quantum internet: A vision for the road ahead, Science **362**, 10.1126/science.aam9288 (2018).

[30] V. Ivády, Longitudinal spin relaxation model applied to point-defect qubit systems, Phys. Rev. B **101**, 155203 (2020).

[31] O. Bulancea-Lindvall, N. T. Son, I. A. Abrikosov, and V. Ivády, Dipolar spin relaxation of divacancy qubits in silicon carbide, npj Computational Materials **7**, 10.1038/s41524-021-00673-8 (2021).

[32] S. Kanai, F. J. Heremans, H. Seo, G. Wolfowicz, C. P. Anderson, S. E. Sullivan, M. Onizhuk, G. Galli, D. D. Awschalom, and H. Ohno, Generalized scaling of spin qubit coherence in over 12, 000 host materials, Proceedings of the National Academy of Sciences **119**, 10.1073/pnas.2121808119 (2022).

[33] M. Ye, H. Seo, and G. Galli, Spin coherence in two-dimensional materials, npj Computational Materials **5**, 44 (2019).

[34] N. Zhao, J.-L. Hu, S.-W. Ho, J. T. K. Wan, and R. B. Liu, Atomic-scale magnetometry of distant nuclear spin clusters via nitrogen-vacancy spin in diamond, Nature Nanotechnology **6**, 242 (2011).

[35] D. Kwiatkowski, P. Szańkowski, and L. Cywiński, Influence of nuclear spin polarization on the spin-echo signal of an nv-center qubit, Phys. Rev. B **101**, 155412 (2020).

[36] W.-L. Ma, G. Wolfowicz, N. Zhao, S.-S. Li, J. J. Morton, and R.-B. Liu, Uncovering many-body correlations in nanoscale nuclear spin baths by central spin decoherence, Nature Communications **5**, 4822 (2014).

[37] E. T. Güldeste and C. Bulutay, Wavelet resolved coherence beating in the overhauser field of a thermal nuclear spin ensemble, Phys. Rev. B **105**, 075202 (2022).

[38] M. Onizhuk and G. Galli, Substrate-controlled dynamics of spin qubits in low dimensional van der waals materials, Applied Physics Letters **118**, 154003 (2021).

[39] S. L. Bayliss, P. Deb, D. W. Laorenza, M. Onizhuk, G. Galli, D. E. Freedman, and D. D. Awschalom, Enhancing spin coherence in optically addressable molecular qubits through host-matrix control, Phys. Rev. X **12**, 031028 (2022).

[40] J. Lee, H. Park, and H. Seo, First-principles theory of extending the spin qubit coherence time in hexagonal boron nitride, npj 2D Materials and Applications **6**, 10.1038/s41699-022-00336-2 (2022).

[41] M. W. Doherty, N. B. Manson, P. Delaney, F. Jelezko, J. Wrachtrup, and L. C. Hollenberg, The nitrogen-vacancy colour centre in diamond, Physics Reports **528**, 1 (2013), the nitrogen-vacancy colour centre in diamond.

[42] J. F. Barry, J. M. Schloss, E. Bauch, M. J. Turner, C. A. Hart, L. M. Pham, and R. L. Walsworth, Sensitivity optimization for nv-diamond magnetometry, Rev. Mod. Phys. **92**, 015004 (2020).

[43] W. Yang and R.-B. Liu, Quantum many-body theory of qubit decoherence in a finite-size spin bath, Phys. Rev. B **78**, 085315 (2008).

[44] M. Onizhuk, K. C. Miao, J. P. Blanton, H. Ma, C. P. Anderson, A. Bourassa, D. D. Awschalom, and G. Galli, Probing the coherence of solid-state qubits at avoided crossings, PRX Quantum **2**, 10.1103/PRXQuantum.2.010311 (2021).

[45] C. E. Bradley, J. Randall, M. H. Abobeih, R. C. Berrevoets, M. J. Degen, M. A. Bakker, M. Markham, D. J. Twitchen, and T. H. Taminiau, A ten-qubit solid-state spin register with quantum memory up to one minute, Phys. Rev. X **9**, 031045 (2019).

[46] See Supplemental Material at [URL] for full details of the simulations, additional data for free nuclear spin, and experimental implementations of single nuclear spin Hahn echo.

[47] H. Seo, A. L. Falk, P. V. Klimov, K. C. Miao, G. Galli, and D. D. Awschalom, Quantum decoherence dynamics of divacancy spins in silicon carbide, Nature Communications **7**, 12935 (2016).

[48] M. Šimėnas, J. O'Sullivan, O. W. Kennedy, S. Lin, S. Fearn, C. W. Zollitsch, G. Dold, T. Schmitt, P. Schüffelgen, R.-B. Liu, and J. J. L. Morton, Near-surface $^{125}\mathrm{te}^{+}$ spins with

millisecond coherence lifetime, Phys. Rev. Lett. **129**, 117701 (2022).

[49] S. M. Jahn, E. R. Canarie, and S. Stoll, Mechanism of electron spin decoherence in a partially deuterated glassy matrix, The Journal of Physical Chemistry Letters **13**, 5474 (2022).

[50] W. Yang, W.-L. Ma, and R.-B. Liu, Quantum many-body theory for electron spin decoherence in nanoscale nuclear spin baths, Reports on Progress in Physics **80**, 016001 (2016).

[51] G. Sharma, T. Gaebel, E. Rej, D. J. Reilly, S. E. Economou, and E. Barnes, Enhancement of nuclear spin coherence times by driving dynamic nuclear polarization at defect centers in solids, Phys. Rev. B **99**, 205423 (2019).

[52] K. M. Salikhov, Y. E. Kandrashkin, and A. K. Salikhov, Peculiarities of free induction and primary spin echo signals for spin-correlated radical pairs, Applied Magnetic Resonance **3**, 199 (1992).

[53] L. Kulik, S. Dzuba, I. Grigoryev, and Y. Tsvetkov, Electron dipole–dipole interaction in ESEEM of nitroxide biradicals, Chemical Physics Letters **343**, 315 (2001).

[54] M. H. Abobeih, J. Cramer, M. A. Bakker, N. Kalb, M. Markham, D. J. Twitchen, and T. H. Taminiau, One-second coherence for a single electron spin coupled to a multi-qubit nuclear-spin environment, Nature Communications **9**, 10.1038/s41467-018-04916-z (2018).

[55] H. P. Bartling, M. H. Abobeih, B. Pingault, M. J. Degen, S. J. H. Loenen, C. E. Bradley, J. Randall, M. Markham, D. J. Twitchen, and T. H. Taminiau, Entanglement of spin-pair qubits with intrinsic dephasing times exceeding a minute, Phys. Rev. X **12**, 011048 (2022).

[56] M. H. Abobeih, J. Randall, C. E. Bradley, H. P. Bartling, M. A. Bakker, M. J. Degen, M. Markham, D. J. Twitchen, and T. H. Taminiau, Atomic-scale imaging of a 27-nuclear-spin cluster using a quantum sensor, Nature **576**, 411 (2019).

[57] R. Guichard, S. J. Balian, G. Wolfowicz, P. A. Mortemousque, and T. S. Monteiro, Decoherence of nuclear spins in the frozen core of an electron spin, Phys. Rev. B **91**, 214303 (2015).

[58] W. M. Witzel, M. S. Carroll, L. Cywiński, and S. Das Sarma, Quantum decoherence of the central spin in a sparse system of dipolar coupled spins, Phys. Rev. B **86**, 035452 (2012).

[59] P. Neumann and J. Wrachtrup, *Quantum Optical Diamond Technologies* (Wiley, 2013) Chap. 9, pp. 277–310.

[60] C. E. Bradley and T. H. Taminiau (private communication), 2023.

[61] C. P. Slichter, *Principles of magnetic resonance* (Springer, 2011).

[62] K. R. K. Rao and D. Suter, Characterization of hyperfine interaction between an nv electron

spin and a first-shell ^{13}C nuclear spin in diamond, Phys. Rev. B **94**, 060101 (2016).

[63] A. Dréau, J.-R. Maze, M. Lesik, J.-F. Roch, and V. Jacques, High-resolution spectroscopy of single nv defects coupled with nearby ^{13}c nuclear spins in diamond, Phys. Rev. B **85**, 134107 (2012).

[64] J. Yun, K. Kim, and D. Kim, Strong polarization of individual nuclear spins weakly coupled to nitrogen-vacancy color centers in diamond, New Journal of Physics **21**, 093065 (2019).

[65] S. J. Balian, G. Wolfowicz, J. J. L. Morton, and T. S. Monteiro, Quantum-bath-driven decoherence of mixed spin systems, Phys. Rev. B **89**, 045403 (2014).

[66] K. R. K. Rao and D. Suter, Level anti-crossings of a nitrogen-vacancy center in diamond: decoherence-free subspaces and 3d sensors of microwave magnetic fields, New Journal of Physics **22**, 103065 (2020).

[67] G. Wang, A. R. Barr, H. Tang, M. Chen, C. Li, H. Xu, J. Li, and P. Cappellaro, Characterizing temperature and strain variations with qubit ensembles for their robust coherence protection (2022).

[68] D. W. Laorenza and D. E. Freedman, Could the quantum internet be comprised of molecular spins with tunable optical interfaces?, Journal of the American Chemical Society 10.1021/jacs.2c07775 (2022).

[69] W. Yang and R.-B. Liu, Quantum many-body theory of qubit decoherence in a finite-size spin bath. ii. ensemble dynamics, Phys. Rev. B **79**, 115320 (2009).

[70] M. Onizhuk and G. Galli, Pycce: A python package for cluster correlation expansion simulations of spin qubit dynamics, Advanced Theory and Simulations **4**, 2100254 (2021).

[71] J. P. Perdew, K. Burke, and M. Ernzerhof, Generalized gradient approximation made simple, Phys. Rev. Lett. **77**, 3865 (1996).

[72] P. Giannozzi, S. Baroni, N. Bonini, M. Calandra, R. Car, C. Cavazzoni, D. Ceresoli, G. L. Chiarotti, M. Cococcioni, I. Dabo, A. D. Corso, S. de Gironcoli, S. Fabris, G. Fratesi, R. Gebauer, U. Gerstmann, C. Gougoussis, A. Kokalj, M. Lazzeri, L. Martin-Samos, N. Marzari, F. Mauri, R. Mazzarello, S. Paolini, A. Pasquarello, L. Paulatto, C. Sbraccia, S. Scandolo, G. Sclauzero, A. P. Seitsonen, A. Smogunov, P. Umari, and R. M. Wentzcovitch, Quantum espresso: a modular and open-source software project for quantum simulations of materials, J. Phys.: Condens. Matter **21**, 395502 (2009).

[73] K. Ghosh, H. Ma, V. Gavini, and G. Galli, All-electron density functional calculations for

electron and nuclear spin interactions in molecules and solids, Phys. Rev. Materials **3**, 043801 (2019).